Food Chemistry 479 (2025) 143852

Contents lists available at ScienceDirect

Food Chemistry

journal homepage: www.elsevier.com/locate/foodchem

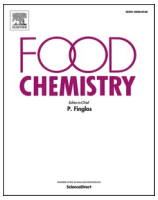

Modulating the electronic configuration of single-atom nanozymes using cobalt nanoclusters for enhanced mycotoxin degradation

Yaqi Zhang [a], Huikang Lin [a], Lan Wang [a], Lijun He [b], Yong Man [b], Bingxuan Jia [a], Zheng Yan [a], Shimo Kang [a], Haijiao Xie [c], Aibo Wu [a,*]

[a] CAS Key Laboratory of Nutrition, Metabolism and Food Safety, Shanghai Institute of Nutrition and Health, University of Chinese Academy of Sciences, Chinese Academy of Sciences, Shanghai 200031, China
[b] School of Chemistry and Chemical Engineering, Henan University of Technology, Zhengzhou 450001, China
[c] Hangzhou Yanqu Information Technology Co., Ltd., Hangzhou 310003, China

ARTICLE INFO

Keywords:
Mycotoxin
Single atoms
Nanoclusters
Modulation
Peroxymonosulfate
Degradation mechanism

ABSTRACT

Herein, Co- and Fe-based single-atom nanozymes (M/N-PC, M = Co or Fe) were successfully fabricated and their catalytic performances for patulin degradation were evaluated systematically. Co/N-PC, consisting of Co–N_4 and nanoclusters sites, achieved a higher patulin degradation efficiency (99.4 %, within 60 min) than Fe/N-PC (only consisting of Fe–N_5 sites). Synergistic interactions between Co–N_4 and Co nanoclusters greatly enhanced electron density near the Fermi level in Co/N-PC, enabling its high catalytic performance. The degradation products of patulin exhibited negligible cytotoxicity. The M/N-PCs demonstrated good reusability, broad pH adaptability and high practical application potential for patulin degradation in apple juice. M/N-PC also exhibited high efficiency in degrading aflatoxin B_1, deoxynivalenol and zearalenone (~100 %, 10–40 min). This study provides in-depth insights into the relationship between metal active site structures in M/N-PCs and their catalytic properties for mycotoxin detoxification, offering guidance for the design of highly efficient single-atom nanozymes.

1. Introduction

Mycotoxins are toxic secondary metabolites produced by filamentous fungi that present significant health risks to humans and animals, including organ toxicity, genotoxicity, immunosuppression, teratogenicity and carcinogenicity (Fu, Yue, Zhang, & Li, 2024). Alarmingly, 60–80 % of agricultural commodities are contaminated with mycotoxins, with 20 % exceeding the European Union's legal food safety limits, posing a significant threat to food safety and public health (Johns, Bebber, Gurr, & Brown, 2022). Various physical, chemical and biological degradation techniques have been developed to reduce the risk of mycotoxin contamination. Among them, enzymes, with health-safe and environmentally friendly properties, are emerging as a promising method for mycotoxin degradation (Xing et al., 2023). Natural metalloenzymes with peroxidase (POD) activity, such as manganese peroxidase, multicopper oxidase and horseradish peroxidase, have been applied in the degradation of mycotoxins (Adegoke et al., 2023; You et al., 2024). However, the drawbacks of high cost, unstable structure in complex environments, and long treatment times seriously restrict the large-scale application of natural enzymes (Zhang et al., 2022).

Nanozymes are promising substitutes for natural enzymes, due to their cost-effectiveness, exceptional stability and high catalytic efficiency (Xu et al., 2022; Yang et al., 2024). Recently, single-atom nanozymes (SAzymes) mimicking POD activity have attracted widespread attention due to their excellent catalytic performance, which has been attributed to their high metal-atom utilization rates, flexible coordination environments, and unsaturated metal coordination (Feng et al., 2021; Li et al., 2021). Single Co atoms exhibit a high spin state enhancing the electron transfer between SAzymes and react substances, and single Fe atoms demonstrate a moderate Gibbs free energy during the singlet oxygen ($^1O_2$) generation step, with both these factors contributing to the excellent catalytic activity of Co- and Fe-based SAzymes (Hu et al., 2023). A previous study showed that in comparison to Co–N_3 and Co–N_4, Co–N_2 increased the electron density of Co atoms, resulting in enhanced activity during bisphenol A degradation (Liang et al., 2022). Additionally, Fe–N_5 exhibited superior adsorption

* Corresponding author.
E-mail addresses: yqzhang@sinh.ac.cn (Y. Zhang), linhuikang2020@sinh.ac.cn (H. Lin), wanglan@sinh.ac.cn (L. Wang), lijunhe@haut.edu.cn (L. He), ribioman@163.com (Y. Man), jiabingxuan2017@sinh.ac.cn (B. Jia), zyan@sinh.ac.cn (Z. Yan), shimokang@sinh.ac.cn (S. Kang), xiehaijiao@shiyanjia.com (H. Xie), abwu@sibs.ac.cn (A. Wu).

https://doi.org/10.1016/j.foodchem.2025.143852
Received 12 December 2024; Received in revised form 18 February 2025; Accepted 10 March 2025
Available online 13 March 2025

energy compared to Fe–N_4, facilitating efficient electron extraction from contaminants and the rapid regeneration of active sites (Du et al., 2024). Therefore, the metal center and the coordination environment of SAzymes determine their pollutant degradation efficiency and mechanism of action, but it is still unknown in the degradation of mycotoxins.

Mycotoxins are characterized as complex multi-ring systems, with specific functional groups (e.g., lactones, ketones, phenolic groups) and significant stereochemical complexity, exhibiting a higher thermal and chemical stability (Feizollahi & Roopesh, 2021; Kolawole, Meneely, Petchkongkaew, & Elliott, 2021). To achieve the efficient degradation of mycotoxins, it is imperative to further enhance the activity of SAzymes. However, the limitations of low metal loadings (usually $\leq$1 %) and lack of synergistic active sites impede traditional SAzymes from surpassing their inherent performance in more complex reactions (Dong et al., 2020; Xu, Liu, & Liu, 2023). Recent advancements have demonstrated that metal nanoclusters can modulate the geometric structure and electronic configurations of metal single atoms, significantly improving their catalytic performance for reactions such as oxygen reduction, oxygen evolution and hydrogen production (Li et al., 2023; Wang et al., 2021). The strong interaction between Co nanoclusters and Co–N_4 sites can increase the valence state of Co atoms and optimize adsorption energy for the oxygen reduction reaction, facilitating O_2 reduction (Wang et al., 2021). Single Mn atoms could synergistically interact with Mn nanoclusters, reducing energy barriers in the reaction pathways and enhancing the reaction kinetics (Li et al., 2023). Moreover, the interactions between single atoms and nanoclusters inevitably affect the molecular structure, bond length, and charge distribution of the molecules in contact with these atoms, further affecting the subsequent degradation behaviour (Hao et al., 2024). Therefore, a comprehensive investigation of the synergistic relationship between single-atoms and nanoclusters is crucial for the rational design of SAzymes for enhancing mycotoxin degradation.

Zeolitic imidazolate framework-8 (ZIF-8) contains an abundance of porous structures and metal atom anchoring sites, making it an ideal platform for the synthesis of SAzymes, in which the concentration of doped metal in ZIF-8 is usually $\leq$2.5 % (Wang et al., 2018; Wu et al., 2023). By moderately increasing the level of metal doping in ZIF-8, nanoclusters can be introduced to SAzymes while maintaining excellent atomic dispersion properties and stability (Wang et al., 2023). Based on these aspects, M/N-PC (M = Co, Fe) were synthesized via the pyrolysis of metal-doped ZIF-8 (M-ZIF-8, with Co and Fe doping rates up to 5 %), allowing M/N-PC to be utilized for the first time as a peroxymonosulfate (PMS) catalyst during the degradation of patulin (PAT). Dual active sites consisting of Co–N_4 and Co nanoclusters were constructed in Co/N-PC, while Fe–N_5 active sites were formed in Fe/N-PC, which effectively catalyzed PMS to generate abundant reactive species to destroy the lactone and hemiacetal structures of PAT. Furthermore, the PAT degradation pathways and the cytotoxicity of degradation products were systematically investigated. The mechanisms of metal single atoms and nanocluster sites in PMS activation were revealed through density functional theory (DFT) calculations. Finally, the practical application potential of M/N-PCs for the degradation of PAT was investigated, as well as their performance in degrading aflatoxin B_1 (AFB_1), deoxynivalenol (DON), and zearalenone (ZEN). This study describes a novel and effective strategy for mycotoxin detoxification and provides theoretical guidance for the synthesis of highly effective SAzymes.

2. Experimental section

2.1. Chemicals

The PAT, AFB_1, DON and ZEN standards were obtained from Pribolab Biological Engineering Co., Ltd. (Qingdao, China). Cobalt nitrate hexahydrate ($Co(NO_3)_2{\cdot}6H_2O$), ferrous sulfate heptahydrate ($FeSO_4{\cdot}7H_2O$) and zinc nitrate hexahydrate ($Zn(NO_3)_2{\cdot}6H_2O$, *p*-benzoquinone (BQ), methyl phenyl sulfoxide (PMSO), dimethylimidazole (2-MeIm) and hydrofluoric acid (HF) were obtained from Titan Co., Ltd. (Shanghai, China). PMS ($2KHSO_5{\cdot}KHSO_4{\cdot}K_2SO_4$) was bought from Sinopharm Chemical Reagent Co., Ltd. (Shanghai, China). Tertiary butyl alcohol (TBA), furfuryl alcohol (FFA), deuterium oxide (D_2O, 99 atom % D), and methyl phenyl sulfone ($PMSO_2$) and potassium thiocyanate (KSCN) were bought from Shanghai Macklin Biochemical Technology Co., Ltd. (China). Human embryonic kidney cell lines (HEK 293T) were purchased from Beina Chuanglian Biotechnology Institute (Beijing, China). Penicillin-streptomycin-amphotericin B and trypsin ethylene diamine tetraacetic acid solution A (EDTA, 0.25 %) were bought from Biological Industries Co., Ltd. (Kibbutz Beit, Israel). Dulbecco's Modified Eagle's Medium (DMEM) with high glucose (SH30243.01) was purchased from HyClone Laboratories Inc. (South Logan, USA). Fetal bovine serum (FBS) was obtained from Invitrogen Co., Ltd. (Waltham, USA).

2.2. Preparation of M/N-PCs

M/N-PC (M = Co, Fe) was synthesized according to the previous report with modifications (Zhang et al., 2022). $Co(NO_3)_2{\cdot}6H_2O$ or $FeSO_4{\cdot}7H_2O$ (0.77 mmol) was mixed with $Zn(NO_3)_2{\cdot}6H_2O$ (14.72 mmol) and dispersed into 450 mL of MeOH, followed by adding 120 mmol of 2-MeIm. Then, the above solution was stirred for 2 h at room temperature. The precipitate was collected, washed with MeOH, and dried in a vacuum oven at 80 °C. The obtained M-ZIF-8 underwent pyrolysis at 900 °C for 2 h in an argon atmosphere. Then, the samples were etched with a 10 % HF for 5 h to eliminate metal nanoparticles. The final M/N-PC was thoroughly washed three times with water and subjected to vacuum freeze-drying for desiccation. In the synthesis of M-ZIF-8, the metal doping levels were maintained at 5 %, representing the molar percentage of M/(Zn + M). For comparative analysis, N-doped porous carbon (N-PC) was obtained by pyrolyzing ZIF-8, which was synthesized under conditions identical to those for M-ZIF-8 but without the incorporation of Co or Fe salts.

2.3. Characterizations of M/N-PCs

The morphologies of the SAzymes were observed using field-emission scanning electron microscopy (SEM, Carl Zeiss Jena, ZEISS Gemini 300, Oberkochen, Germany), transmission electron microscopy (TEM) and a high-resolution transmission electron microscopy (HRTEM, JEOL, JEM F200, Tokyo, Japan). Aberration-corrected high-angle annular dark-field scanning transmission electron microscopy (AC-HAADF-STEM) was performed on a Themis Z platform, equipped with double aberration correctors and a cold field emission gun operated at 80 kV (Thermo Fisher Scientific, Waltham, USA). The specific surface area and pore configuration of the obtained materials were investigated through nitrogen adsorption-desorption isotherms using an automatic specific surface and porosity analyzer (Micromertics, ASAP 2460, Atlanta, USA). X-ray diffraction (XRD) spectra were recorded by an X-ray diffractometer (Malvern Panalytical, X'Pert3 Powder, Almelo, Holland) using Cu Kα radiation at 40 kV and 30 mA. Raman and in-situ Raman spectra were obtained on a Raman spectrometer (HORIBA Jobin Yvon, LabRAM HR Evolution, Paris, France) with an excitation wavelength of 532 nm. X-ray photoelectron spectroscopy (XPS) patterns were detected using an X-ray photoelectron spectrometer (Thermo Fisher Scientific, K-Alpha, Waltham, USA). Co and Fe K-edge X-ray absorption fine structure (XAFS) analysis were performed with Si (111) crystal monochromators at the BL11B beamlines at the Shanghai Synchrotron Radiation Facility (SSRF) (Shanghai, China). Co and Fe K-edge extended X-ray absorption fine structure (EXAFS) spectra were recorded in transmission mode. The EXAFS data analysis and fitting were performed using the Athena and Artemis software. The metal contents of M/N-PCs were analyzed by inductively coupled plasma mass spectrometry (ICP-MS, Agilent, 7700X, Santa Clara, USA). Electron paramagnetic resonance (EPR) spectra were obtained on a Bruker EPR EMXplus-6

spectrometer (Rheinstetten, Germany). Electrochemical tests were performed in a standard three-electrode system using a CHI 760E electrochemical workstation.

2.4. Degradation experiments and analytical methods of mycotoxins

M/N-PC was added to the mycotoxin aqueous solution (20 mL, 2.5 mg/L), and the degradation reaction was initiated by the addition of PMS. The mixture was agitated at room temperature under dark conditions. Samples were taken at predetermined time intervals and subjected to analysis after being filtered through a 0.22 μm syringe filter. For recyclability tests, the SAzymes were recovered by centrifugation, thoroughly washed with acetonitrile and water, and freeze-dried to remove solvent and moisture before being reused for subsequent cycles under identical conditions.

The concentrations of mycotoxins were determined using high-performance liquid chromatography (HPLC, Thermo Fisher Scientific, UltiMate 3000, Waltham, USA). Chromatographic separations of mycotoxins were performed on a C18-column (250 mm × 4.6 mm, 5 μm). A compound solution of water-acetonitrile was used as the mobile phase, and the flow rate was set at 1.0 mL/min. The volume ratios of water-acetonitrile for PAT, AFB_1, DON and ZEN were 90:10, 35:65, 75:25 and 25:75, respectively. The column temperature was maintained at 40 °C. The detection wavelengths were specifically set at 274 nm, 362 nm, 218 nm and 230 nm for PAT, AFB_1, DON and ZEN, respectively. The injection volume was set as 20 μL.

2.5. Analytical methods of PAT degradation products

The degradation products were extracted as follows. The M/N-PC was separated from the reaction system. An excess sodium chloride was added to the supernatant to form a supersaturated solution. Acetonitrile was then added, and the mixture was vortexed for 5 min. The mixture was centrifuged at 5000 rpm for 10 min, and the supernatant was collected. This extraction process was repeated three times. The separated M/N-PC was washed with acetonitrile three times. An excess sodium chloride was added to the obtained acetonitrile, and the above extraction steps were repeated. All supernatants were combined and concentrated to near dryness under a nitrogen stream at 50 °C. The residue was dissolved in 1 mL of acetonitrile and filtered through a 0.22 μm PTFE syringe filter for analysis.

The degradation products of PAT were analyzed using liquid chromatography-tandem mass spectrometry (LC-MS/MS). This was achieved by coupling a SHIMADZU Nexera UHPLC system (Kyoto, Japan) to an AB-SCIEX 6600 Triple TOF-MS spectrometer (Waltham, USA). The chromatographic column used was a T3 column (2.1 × 100 mm, 1.8 μm). The mobile phase consisted of 5 mmol/L ammonium acetate in water (phase A) and methanol (phase B), with a flow rate of 0.3 mL/min. The elution procedure was programmed as follows: 0–3 min, 100 % phase A; 3–12 min 50 % phase A; 12–15 min, 10 % phase A; 15–18 min, 100 % phase A. The detection conditions of mass spectrometry were set as follows: negative ion mode; TOF-MS 50–500 *m/z*; ion source: Duo Spray Ion Source; ion source gas 1:50 psi; curtain gas: 35 psi; temperature: 400 °C; ISVF: −4500 V; declustering potential: −80.0 eV; collision energy: −28.0 eV; accumulation time: 0.1 s.

2.6. Cell culture and toxicity assay

The HEK 293T cells were cultured in a growth medium of DMEM containing 10 % FBS and 1 % penicillin-streptomycin-amphotericin B. The cells were maintained in a humidified incubator under a 5 % CO_2 atmosphere. Toxicity assays were carried out in 96-well plates with 15,000 HEK 293T cells plated per well. After an initial 24 h incubation period to allow cell attachment and spreading, the growth medium was aspirated and replaced with fresh DMEM containing a range of PAT concentrations (0, 2.5, 5, 10, and 20 μmol/L), the catalytic degradation products of PAT, and the supernatant from the catalytic system. Following medium replacement, the cells were cultured for an additional 24 h. Cell viability was evaluated using the CCK-8 assay kit (Dojindo, Japan), with optical density (OD) measured at 450 nm using a microplate reader (GENios Pro, Tecan, Männedorf, Switzerland).

2.7. Computational methods

The energy gap between PAT and active species was calculated using Gaussian 16 software. The PBE0 functional was adopted for all calculations in combination with D3BJ dispersion correction. Geometry optimization, frequency and singlet point energy calculations were performed using the def2SVP basis set, with a polarizable continuum model, considering water as the solvent. The Fukui function was calculated using Multiwfn v.3.8 (dev).

A two-dimensional (2D) model of the Co-N_4/Co cluster was constructed by loading single Co atoms and Co clusters onto pyridinic N-doped graphene. Similarly, a 2D model of Fe–N_5 was constructed by incorporating single Fe atoms and pyridine axial ligands onto pyridinic N-doped graphene. Structural optimizations were performed using Vienna Ab-initio Simulation Package (VASP) software with the projector augmented wave method. The exchange-correlation function was treated using the Perdew-Burke-Ernzerhof function in combination with DFT-D3 correction. A plane-wave basis set cut-off energy of 450 eV was applied. For the optimization of lattice sizes in 2D models, Brillouin zone integration was performed with a Gamma *k*-point sampling of 1 × 1 × 1 and self-consistent calculations were applied with a convergence energy threshold of 10^{-5} eV. The equilibrium geometries and lattice constants were optimized with a maximum stress criterion of 0.02 eV/Å for each atom. The isosurface level for charge density difference was set at 0.005 e/Å^3. The spin polarization method was used to describe the magnetism of models. The adsorption energy of PMS was determined using Eq. (1) as follows:

$$E_{ads} = E_{(A)} - E_{(B)} - E_{(PMS)} \quad (1)$$

where, $E_{(A)}$ is the total energy of 2D models with PMS adsorbed; $E_{(B)}$ is the total energy of the 2D model alone; and $E_{(PMS)}$ is the total energy of PMS in gas phase. The configuration of PMS was optimized within a 20 × 20 × 20 Å^3 box. The density of states of the 2D model was calculated using the GGA-PBE functional and then treated by the VASPKIT interface.

2.8. Practical application performance in apple juice

The practical potential of M/N-PC for degrading PAT in apple juice was evaluated. Apples from two different regions, Shandong (No. 1) and Shanxi (No. 2), as well as apple juices from four commercial brands (No. 3 Hui Yuan, No. 4 Wei Quan, No. 5 EWEN and No. 6 Fontana), were bought from a local supermarket in Shanghai (China). Freshly pressed apple juice was prepared through the following steps: the apples were washed, peeled and cut into quarters, then seeds and stems were removed. The juice was extracted using a household juicer (JC307, Supor, Shanghai, China) and filtered through four layers of muslin to remove any remaining solid or fiber debris. Following this, the juice was centrifuged at 4000 rpm for 10 min at 4 °C to remove impurities and coarse particles. The freshly pressed apple juice was stored at −20 °C. PAT was not detected in any of the samples. The spiked apple juice samples were prepared by directly adding the PAT standard solution to samples. The degradation experimental progress was analogous to that applied for PAT aqueous solution.

To extract PAT from apple juice, 2.0 mL of ethyl acetate was added to a 2.0 mL sample of apple juice and the mixture was vigorously shaken for 2 min. The organic phase was then carefully separated and transferred to a clean test tube. The aqueous phase was subjected to the extraction process twice more using ethyl acetate and the resulting

solutions were combined with the organic phase. The combined organic phase samples were then shaken and filtered by adding 200 mg of anhydrous sodium sulfate. The filtrate was dried under a nitrogen atmosphere and then dissolved in 2.0 mL of acetonitrile. Finally, the solution was filtered through a 0.22 μm syringe filter and analyzed by HPLC.

3. Results and discussion

3.1. Synthesis and characterization of M/N-PC

A schematic of the process used for M/N-PC synthesis is shown in Fig. 1a. The precursor of M-ZIF-8 was prepared by combining Zn^{2+} and 2-MeIm organic ligand dopants, with the simultaneous partial substitution of Zn^{2+} by Co^{2+} or Fe^{2+} at specific molar ratios. M/N-PCs were obtained through the pyrolysis of M-ZIF-8 at 900 °C under an argon atmosphere. Zn evaporated during the pyrolysis process, providing additional free nitrogen sites, effectively preventing metal species

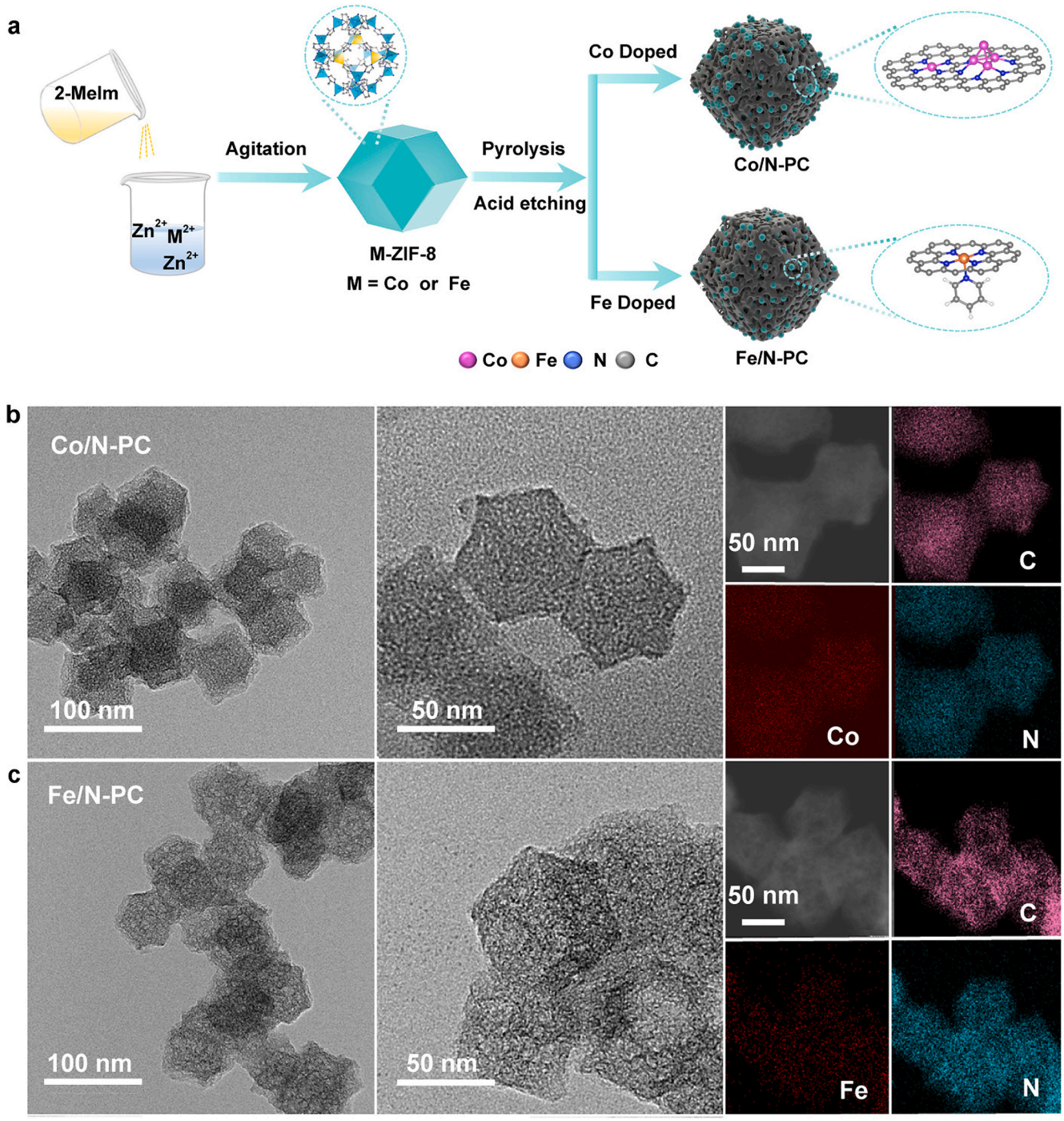

Fig. 1. (a) Schematic illustration of the synthesis process for M/N-PC. (b,c) TEM images and corresponding elemental mapping for C, N and metal atoms in Co/N-PC (b) and Fe/N-PC (c).

aggregation and promoting their atomic dispersion onto the nitrogen-doped carbon substrate (Wang et al., 2023). Both Co-ZIF-8 and Fe-ZIF-8 maintained the original rhombic dodecahedral shape of ZIF-8 (Fig. S1). After pyrolysis, the morphologies of Co/N-PC and Fe/N-PC crystals retained a similar structure to N-PC, with a highly uniform dispersion of Co, Fe, N and C in M/N-PC (Fig. 1b and c, Fig. S2). HRTEM revealed that N-doped carbon supports were highly disordered with numerous vacancies and dislocations, which was beneficial to the anchoring of metal atoms (Fig. S3) (Feng et al., 2021).

In the XRD patterns of Fe/N-PC, no diffraction peaks associated with the metal crystal phase were observed, indicating that Fe existed as isolated atoms (Fig. S4a) (Wu et al., 2023). For Co/N-PC, two weak peaks located at 44.3° and 51.4° were assigned to the (111) and (200) planes of zero-valent cubic-phase cobalt (Co^0) (Xiao et al., 2023). As large Co nanoparticles could be removed by acid etching and were not observed in TEM images, crystalline metallic Co nanoclusters might form in Co/N-PC (Wang et al., 2021). The intensity ratios of the D band and G band (I_D/I_G) exceeded 1.0 in the Raman spectra, reflecting a high abundance of defects in M/N-PC samples, which can enhance their catalytic activity by promoting interfacial electron transfer between active sites and PMS (Fig. S4b) (Feng et al., 2021; Hu, Huang, & Peng, 2023). All samples exhibited a type IV isotherm and had high specific surface areas ranging from 666.9 to 886.6 m^2/g, with the measured pore size being able to provide access to the PAT molecule (0.88 nm × 0.77 nm) (Fig. S4c and d, Table S1). The presence of a highly porous structure and large specific surface area in M/N-PC would facilitate the utilization

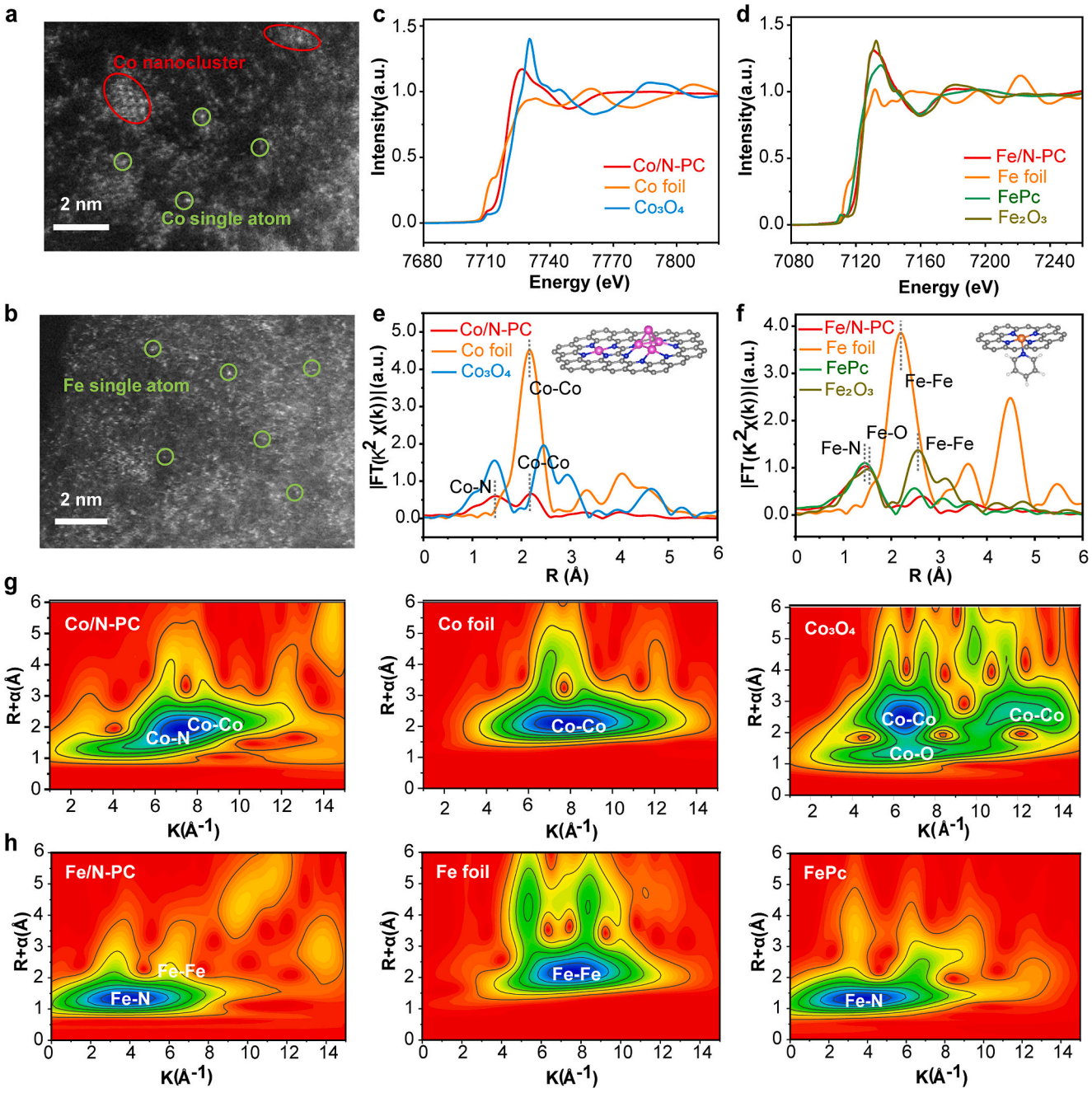

Fig. 2. (a,b) AC-HAADF-STEM images of Co/N-PC (a) and Fe/N-PC (b). (c, d) Co K-edge and Fe K-edge XANES spectra of Co/N-PC (c) and Fe/N-PC (d). (e,f) FT-EXAFS fitting curves of Co/N-PC (e) and Fe/N-PC (f), insets show the schematic atomic structure of Co/N-PC and Fe/N-PC (Co: pink, Fe: orange, N: blue, C: gray and H: white). (g,h) WT analysis at the Co K-edge for Co/N-PC (g) and the Fe K-edge for Fe/N-PC (h). (For interpretation of the references to colour in this figure legend, the reader is referred to the web version of this article.)

of active sites and reduce the mass transfer path for reactants (Zhang, Sun, et al., 2022).

The elemental composition of the near-surface region of M/N-PCs and the related valence states were examined by XPS. According to the survey spectra shown in Fig. S5a, C, N, O, and Zn elements were detected in both Co/N-PC and Fe/N-PC. The intensities of Co and Fe were low due to the limited analysis depth of XPS (<10 nm) (Zhang, Cui, et al., 2022). The high-resolution XPS N 1 s spectra of all samples were deconvoluted into four peaks, corresponding to pyridinic N (~398.6 eV), pyrrolic N (~399.6 eV), graphitic N (~400.9 eV) and oxidized N (~403.2 eV) (Fig. S5b) (Chen et al., 2023; Liang, Wang, et al., 2022; Zhang, Cui, et al., 2022). Pyridinic N likely coordinated with dispersed metal atoms to form M-N_x and the binding energies of pyridinic N and M-N_x were relatively close, making them difficult to distinguish (Liu et al., 2023). The high-resolution XPS Fe 2p spectrum showed only positively charged metal species without any zero-valence species, indicating that Fe species had likely coordinated with pyridinic N as single atoms in Fe/N-PC (Fig. S5c). The high-resolution Co 2p spectrum contained Co^{2+}, Co^{3+} and Co^0, showing that both Co-N_x and Co nanoclusters existed in Co/N-PC. In Co/N-PC and Fe/N-PC, the weight percentages of Co and Fe were 3.23 and 1.13 %, respectively. The observed differences in metal doping levels were attributed to the different interaction strengths between metal atoms and 2-MeIm (Li et al., 2023; Wu et al., 2023).

The atomic level structural features of metal species in Co/N-PC and Fe/N-PC were further elucidated. The bright white spots in green circles and red ellipses in AC-HAADF-STEM images corresponded to Co single atoms and Co nanoclusters in Co/N-PC, respectively (Fig. 2a). For Fe/N-PC, numerous isolated bright dots were visible, with no Fe nanoclusters observed, showing isolated Fe single atom distribution (Fig. 2b). The electronic structure and coordination environment of Co and Fe species in Co/N-PC and Fe/N-PC were analyzed by X-ray absorption near edge structure (XANES) spectroscopy and extended X-ray absorption fine structure (EXAFS). Based on the XANES spectra at the Co K-edge and Fe K-edge, the valence states of Co ranged between 0 and 3 (Fig. 2c), while for Fe they ranged between 2 and 3 (Fig. 2d). The Fourier-transformed (FT) k^3-weighted EXAFS spectrum of Co/N-PC contained two peaks at approximately 1.4 Å and 2.2 Å, corresponding to the scattering paths of Co–N and Co–Co, respectively (Fig. 2e). As shown in Fig. 2f, a prominent peak was observed in the FT k^3-weighted EXAFS spectrum of Fe/N-PC, located at approximately 1.4 Å in the initial coordination shell of Fe. This peak aligned with the Fe–N scattering path of iron phthalocyanine (FePc) (Mo et al., 2023). Additionally, a minor peak observed at approximately 2.7 Å deviated from the metal scattering path of Fe–Fe in Fe foil and Fe_2O_3, indicating the absence of Fe–Fe in Fe/N-PC (An et al., 2018; Peng, Duan, Shang, Gao, & Xu, 2021). Wavelet transform (WT) contour plots visually depicted Co–N and Co–Co scattering in Co/N-PC as well as Fe–N interactions in Fe/N-PC, which was consistent with the results of FT-EXAFS analysis (Fig. 2g and h, Fig. S6). Furthermore, least-squares fitting of EXAFS data at the Co K-edge and Fe K-edge in R-space was conducted to determine the structural parameters of Co and Fe. The average coordination numbers of Co–N and Co–Co were determined to be 4.1 and 1.7, respectively in Co/N-PC (Table S2). In case of Fe/N-PC, the coordination number of Fe–N was determined to be 5.3, which was in the range of Fe–N_5 coordination with the wobbling effect of a fifth ligand (Table S3) (Wu et al., 2023). Despite the fitting results indicating the presence of Fe–Fe, the Debye-Waller factor (σ^2) of Fe–Fe was significantly higher than that of Fe foil and Fe oxides, indicating a higher degree of disorder in Fe–Fe bonds, which were potentially formed from the thermal migration and coalescence of high-density isolated Fe–N_5 species (Xia et al., 2022). The EXAFS fitting curves of Co/N-PC and Fe/N-PC were both well-fitted with the backscattering paths of Co–N_4 and Co–Co, as well as Fe–N_5, respectively (Fig. S7). Combined with XPS, XRD and AC-HAADF-STEM results, it was confirmed that single Co atoms and Co nanoclusters coexisted in Co/N-PC, while only single Fe atoms existed in Fe/N-PC, providing highly efficient active sites for PMS activation (Li et al., 2022).

3.2. Correlation between metal sites and catalytic activity

The catalytic activity of M/N-PC was evaluated by employing PAT as a model. The prepared catalysts (0.25 mg) exhibited PAT adsorption efficiencies ranging from only 9.4 % to 24.1 %, indicating low levels of PAT adsorption (Fig. 3a). Additionally, PMS was unable to directly oxidize PAT (Fig. 3b). When PMS was activited by Co/N-PC and Fe/N-PC, the degradation efficiencies of PAT increased to 99.4 % and 34.6 %, respectively (Fig. 3b). In contrast, the utilization of N-PC did not significantly enhance the PAT removal efficiency. The degradation kinetics of PAT were further evaluated using the pseudo-first-order kinetics model, and the rate constants k (min^{-1}) of each catalyst are shown in Fig. 3c. Among all the prepared SAzymes, Co/N-PC achieved the highest k value (0.084 min^{-1}). The superior catalytic activity of Co/N-PC may be attributed to the incorporation of Co nanoclusters, which induced charge redistribution within Co–N_4 sites, thereby strengthening the interaction between Co–N_4 and PMS (Mo et al., 2023). To further identify the catalytic potential of Fe/N-PC and N/PC in PMS activation, the effect of dosage on PAT removal efficiency was investigated. The PAT degradation efficiency progressively increased with the addition of higher catalyst dosages, increasing by 62.7 % with the addition of 1.0 mg of Fe/N-PC, relative to their corresponding adsorption efficiencies (Fig. 3d and Fig. S8). This enhancement in PAT removal efficiency was primarily ascribed to the catalytic degradation process. In contrast, the PAT degradation efficiency of N-PC increased by only 2.6 %, showing that N-PC had a negligible role in PAT degradation, possibly due to the difficulty of PMS molecule adsorption onto N–C sites (Gao et al., 2021).

3.3. PAT degradation pathways and the cytotoxicity of degradation products

The Fukui index was used to identify groups targeted by various reactive species, quantitatively assessing the reactivity of each atom in the PAT molecule. Atoms exhibiting high $f(-)$ values are most reactive towards electrophilic species, such as $^1O_2$, while $f(0)$ values indicate regioselectivity for hydroxyl radical (·OH) and sulfate radical ($SO_4^{\bullet-}$) (Wang, Xiong, et al., 2023). As shown in Fig. 4a, electrophilic reactions were predominantly centered at C (2), C (8) and O (15) due to their high $f(-)$ values, making them susceptible to attack by $^1O_2$. Furthermore, C (2), C (3), C (4), C (8) and O (15) had elevated $f(0)$ values, indicating that these atoms were vulnerable to free radical attack (Hu, Huang, & Peng, 2023). The PAT degradation products formed in the M/N-PC/PMS catalytic systems were identified via liquid chromatography-mass/mass spectrometry (LC-MS/MS) and their respective structures were proposed based on the Fukui index results (Fig. S9 and 10). The potential degradation pathways for PAT are illustrated in Fig. 4b. In pathway I, the C(2) site of PAT was oxidized by reactive species, followed by the cleavage of the pyran ring, resulting in the formation of product P1 (Meng et al., 2024; Qiu et al., 2024). The furan ring of P1 was subsequently cleaved via hydrolysis, oxidation, and decarboxylation, ultimately yielding P2 (Fig. S11a) (Hu, Huang, & Peng, 2023; Qiu et al., 2024). In the Co/N-PC/PMS system, P1 was likely completely converted to P2 under the strong oxidation conditions. In pathway II, the hydroxyl group on the C(5) site of PAT was oxidized, followed by hydrolysis, decarboxylation, and oxidation of the furan ring in the Co/N-PC/PMS system, forming product P3 (Fig. S11b) (Hu, Huang, & Peng, 2023; Wei et al., 2024). Pathway III involved the formation of product P4 in both the Co/N-PC/PMS and Fe/N-PC/PMS systems (Fig. S11c). Similar to pathway II, the hydroxyl group on the C(5) site was oxidized, followed by hydrolysis of the C(4)-C (5) bond in PAT, resulting in the formation of $C_7H_6O_5$ (Maneeboon, Roopkham, Mahakarnchanakul, & Chuaysrinule, 2024). Subsequently, P4 was generated via the formate hydrolysis reaction.

PAT is known to target the kidney, potentially inducing nephrotoxicity (Ramalingam, Bahuguna, & Kim, 2019). Therefore, the cytotoxicity

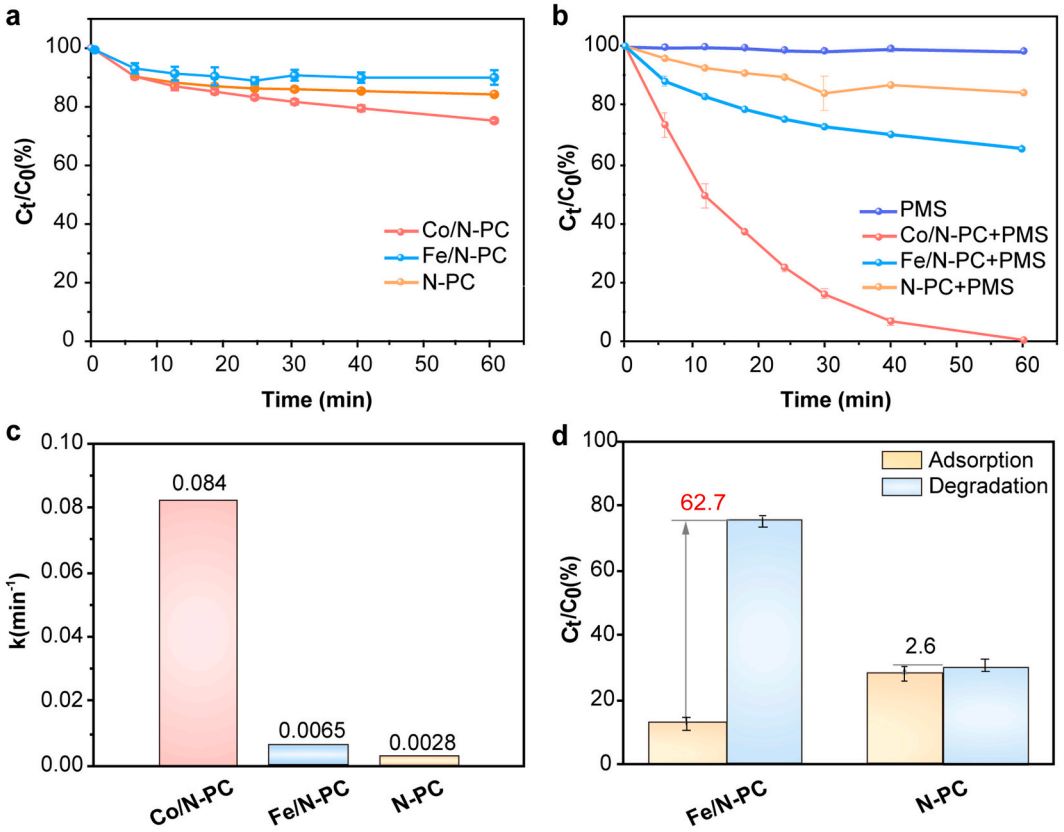

Fig. 3. (a-c) Comparison of PAT adsorption (a) and degradation (b) efficiencies in different M/N-PC systems for PAT, and the corresponding degradation rate constants (c). Conditions: [Cat.] = 12.5 mg/L, [PMS] = 3.0 mmol/L, [PAT] = 2.5 mg/L, initial pH = 7.0. (d) PAT removal efficiency using 50 mg/L of SAzymes. Conditions: [PMS] = 3.0 mmol/L, [PAT] = 2.5 mg/L, initial pH = 7.0.

of PAT degradation products and the catalytic systems was assessed using HEK 293T cells. The viability of HEK 293T cells decreased in a concentration-dependent manner as the concentration of PAT increased from 0 to 20 μmol/L (Fig. S12a). Compared to the control group treated with 5 μmol/L PAT (62.6 % viability), the viability of HEK 293T cells remained at 97.8 % and 99.7 % following treatment using the Co/N-PC and Fe/N-PC catalytic systems, respectively. These results indicated that PAT degradation products induced significantly lower cytotoxicity in HEK 293T cells (Fig. 4c). Previous studies have identified the hemiacetal and lactone ring as the key toxic sites of PAT (Diao, Hou, Hu, Dong, & Li, 2018; Qiu et al., 2024; Wang et al., 2022). Based on the structure-bioactivity relationships, the destruction of the lactone and furan ring significantly reduces the toxicity of PAT (Diao et al., 2018). This structural degradation likely explains the observed reduction in cytotoxicity of the PAT degradation products. Furthermore, the supernatants from both the M/N-PC and M/N-PC/PMS systems had no observable effect on the viability of HEK 293T cells (Fig. 4d and Fig. S12b). Similar trends in the total number of HEK 293T cells treated with different M/N-PC/PMS systems were confirmed by inverted microscopy (Fig. S13). These results demonstrate that the proposed M/N-PC/PMS system is a promising method for PAT removal and detoxification.

3.4. Reactive species and active site identification

To efficiently apply different M/N-PCs for the catalytic degradation of PAT, it is critical to understand the molecular origin of the ranked sequence of reactivity (Co/N-PC > Fe/N-PC). Thus, reactive species formation was initially verified by EPR spectroscopy, using 5,5-dimethyl-1-pyrroline N-oxide (DMPO) and 2,2,6,6-tetramethyl-4-piperidinol (TEMP) as trapping agents for ·OH / $SO_4^{\bullet-}$ and $^1O_2$ in water, respectively. Unlike the signals of DMPO-·OH or DMPO-$SO_4^{\bullet-}$ adducts, distinct characteristic patterns of 5,5-dimethyl-1-pyrrolidone-N-oxyl (DMPOX) were observed in all catalytic systems, resulting from the over-oxidation of DMPO by excessive amounts of ·OH, $SO_4^{\bullet-}$ or $^1O_2$ (Fig. 5a) (Liu et al., 2024)). As shown in Fig. 5b, the 1:1:1 triplet signal of TEMP-$^1O_2$ indicated the generation of $^1O_2$ in the M/N-PC/PMS systems. Additionally, both catalytic systems exhibited the presence of permanent free radicals (PFRs) signals (Fig. S14). PFRs can transfer electrons to molecular oxygen to produce superoxide anion ($O_2^{\bullet-}$), which subsequently self-react to release $^1O_2$ (Y. Zhang, Cui, et al., 2022). The DMPO-$O_2^{\bullet-}$ signal was detected in the M/N-PC/PMS systems (Fig. 5c), confirming the generation of $O_2^{\bullet-}$.

Further quenching experiments were conducted to identify the types of reactive species involved in PMS activation by M/N-PC. MeOH containing α-H can effectively capture ·OH and $SO_4^{\bullet-}$, while TBA without α-H serves as a scavenger for ·OH only (Du et al., 2024; Wu et al., 2023). In the Co/N-PC catalytic system, PAT degradation was slightly inhibited by MeOH, indicating the presence of $SO_4^{\bullet-}$ (Fig. 5d and Fig. S15a). In contrast, in the Fe/N-PC catalytic systems, PAT degradation was inhibited by TBA to a similar extent as MeOH, suggesting that ·OH may play a certain role in this system (Fig. 5d and Fig. S15b). However, both $SO_4^{\bullet-}$ and ·OH exhibited limited effects on PAT degradation, suggesting these were not the main active species responsible for the PAT degradation process. FFA is a scavenger for $^1O_2$ and when added to the system, the PAT degradation process was nearly entirely suppressed, implying that $^1O_2$ was the major reactive species in both Co/N-PC and Fe/N-PC systems (Zhou et al., 2021). It has widely been reported that D_2O can enhance the efficiency of $^1O_2$ oxidation processes by prolonging the lifetime of $^1O_2$ by approximately 18-fold (68 ± 1 μs in D_2O vs. 3.7 ± 0.4 μs in H_2O) (Liu et al., 2024). PAT degradation efficiencies and rates were higher in D_2O than H_2O in all catalytic systems (Fig. S16). When BQ was used as a scavenger for $O_2^{\bullet-}$, the PAT degradation efficiencies decreased

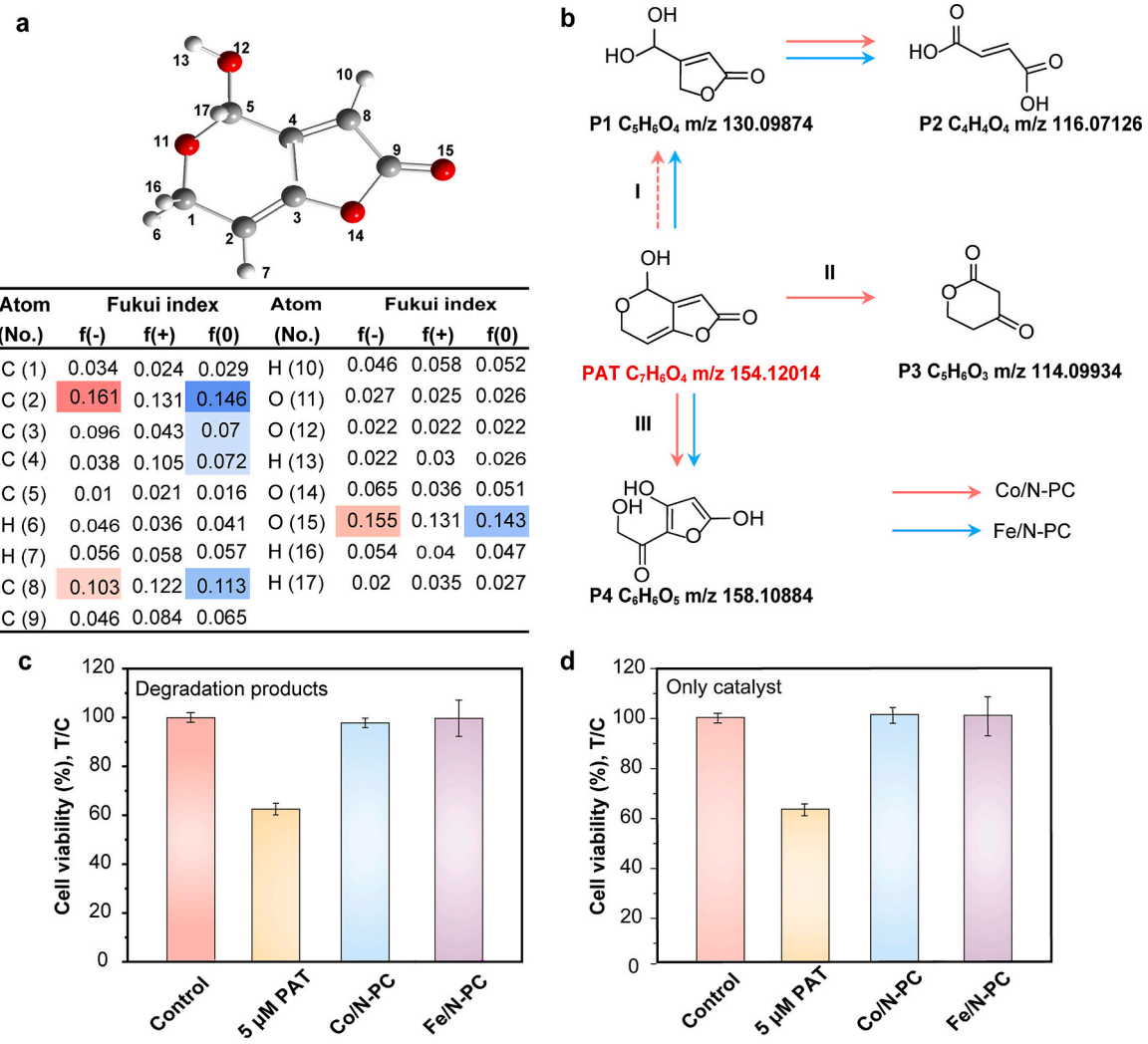

Atom (No.)	Fukui index f(-)	f(+)	f(0)	Atom (No.)	Fukui index f(-)	f(+)	f(0)
C (1)	0.034	0.024	0.029	H (10)	0.046	0.058	0.052
C (2)	0.161	0.131	0.146	O (11)	0.027	0.025	0.026
C (3)	0.096	0.043	0.07	O (12)	0.022	0.022	0.022
C (4)	0.038	0.105	0.072	H (13)	0.022	0.03	0.026
C (5)	0.01	0.021	0.016	O (14)	0.065	0.036	0.051
H (6)	0.046	0.036	0.041	O (15)	0.155	0.131	0.143
H (7)	0.056	0.058	0.057	H (16)	0.054	0.04	0.047
C (8)	0.103	0.122	0.113	H (17)	0.02	0.035	0.027
C (9)	0.046	0.084	0.065				

Fig. 4. (a) Fukui index of each atom in the PAT molecule. (b) Possible PAT degradation pathways in M/N-PC/PMS systems. (c,d) Viability of HEK 293T cells exposed to PAT degradation products (c) and M/N-PC supernatant (d).

to 46.6 % and 62.7 % in the Co/N-PC and Fe/N-PC systems, respectively, implying that $O_2^{\bullet-}$ played a certain role in the degradation of PAT (Du et al., 2024). PMSO can be oxidized by high-valent metal-oxo species, such as Co(IV) = O and Fe(IV) = O, to produce an equivalent amount of $PMSO_2$ (Hu, Zou, et al., 2023; Wang & Wang, 2023). Therefore, PMSO was employed as a probe to detect the generation of high-valent metal-oxo species. As illustrated in Fig. S17, the levels of PMSO consumption and $PMSO_2$ generation in M/N-PC systems were lower than those in the PMS-only system. This observation indicated that high-valent metal-oxo species were not formed during the activation of PMS by M/N-PCs (Yang, Yang, An, & Wang, 2023; Yin et al., 2023).

To gain further insight into the chemical reactivity between active species and PAT, the energy gap (GAP) was calculated between the lowest unoccupied molecular orbital (LUMO) of the active species and the highest occupied molecular orbital (HOMO) of PAT. Active species can typically be categorized as electrophilic radicals, implying their LUMO tends to proactively interact with the HOMO of PAT (Hu, Huang, & Peng, 2023). The ranked order of GAP values between the LUMO of active species and the HOMO of PAT was as follows: $^1O_2$ (2.77 eV) < $SO_4^{\bullet-}$ (3.19 eV) < ·OH (3.62 eV) < $O_2^{\bullet-}$ (8.35 eV) (Fig. 5e), suggesting that PAT was most readily influenced by $^1O_2$. In contrast, due to a substantial GAP between the LUMO of $O_2^{\bullet-}$ and the HOMO of PAT, $O_2^{\bullet-}$ was less able to directly degrade PAT. Thus, $O_2^{\bullet-}$ likely served as a main precursor for $^1O_2$ instead. Based on these findings, it can be concluded that $^1O_2$ was primarily responsible for reactive degradation in all three systems, while $SO_4^{\bullet-}$ and ·OH played minor roles.

Another possible pathway involves nonradical PMS activation, forming a surface-activated complex that directly oxidizes organic molecules via electron transfer. In this process, PMS attaches to the surface of catalyst and forms a highly reactive metastable complex, which subsequently oxidizes the adsorbed target through electron migration (Hu, Huang, & Peng, 2023). As shown by in-situ Raman spectroscopy, when Co/N-PC catalysts were added to the PMS solution, a novel peak appeared at 841 cm^{-1} corresponding to activated peroxide (PMS*), indicating the formation of metastable surface-adsorbed intermediates (Fig. 5f) (Yin et al., 2023). However, no peak indicating PMS* was detected after the introduction of Fe/N-PC, possibly due to the low concentration of produced peroxide PMS*. Chronoamperometry (i-t) curves demonstrated an immediate increase in current densities upon adding PMS, suggesting that with the formation of metastable surface-adsorbed intermediates, electrons were transferred from M/N-PC to PMS (Fig. 5g). The increase in current density after adding Co/N-PC was larger than that of Fe/N-PC, which was consistent with the results of in-situ Raman analysis. Nevertheless, the increase in current density after the addition of PAT was negligible, suggesting limited electron transfer between PAT and metastable surface-absorbed intermediates and thus indicating that the electron-transfer process did not play a major role in PAT degradation. Additionally, KSCN with strong metal-chelating

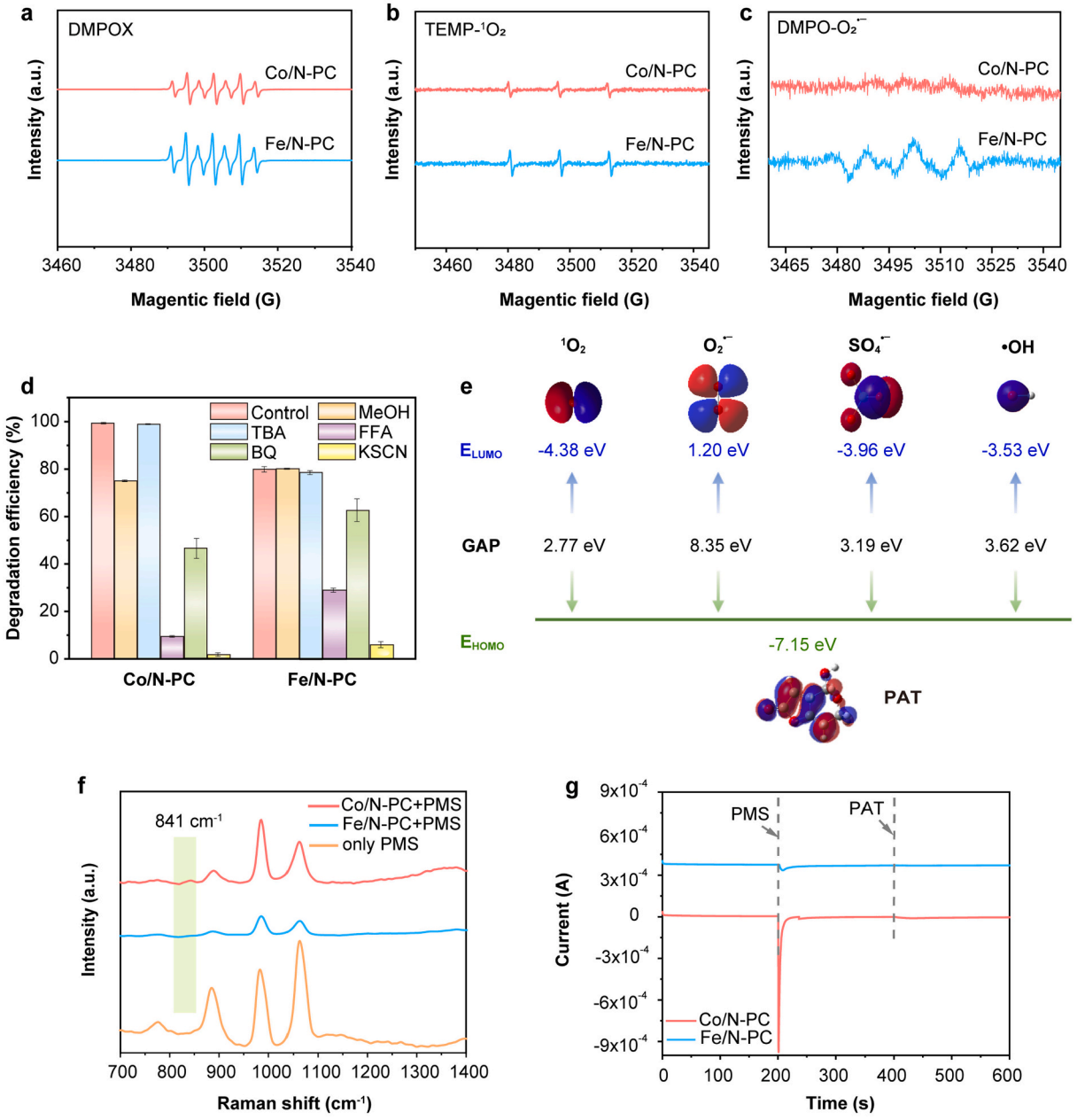

Fig. 5. (a-c) EPR spectra of DMPOX (a), TEMP-$^1O_2$ (b) and DMPO-$O_2^{\bullet-}$ (c). (d) PAT degradation efficiencies in the presence of scavengers. (e) Energy gap between the LUMO of different reactive species and the HOMO of PAT. (f) In-situ Raman spectra of different catalytic systems. (g) Current responses following the sequential addition of PMS and PAT in different catalytic systems.

capability significantly inhibited PAT degradation, confirming that the metal atomic center acted as an active site for interactions with reactants (Fig. 5d and Fig. S15) (Zhu et al., 2023).

3.5. *Theoretical investigations into the catalysis mechanism*

The optimized geometric structures of Co–N_4, Co nanocluster and Fe–N_5 on N-doped graphene, as well as the adsorption configurations of PMS on these active sites, are demonstrated in Fig. S18 and S19, respectively. As shown in Fig. 6a, the negative adsorption energies (E_{ads}) of PMS on various active sites suggested that the process of PMS adsorption onto the catalysts was favorable. The terminal O atom in PMS was more easily adsorbed on single metal atom sites due to its more negative E_{ads} than the peroxy O atom in PMS, while both the terminal and peroxy O atoms were adsorbed on the Co nanocluster. The E_{ads} value (−3.50 eV) of PMS on the Co nanocluster was more negative than that on other sites, suggesting that the Co nanocluster site had the highest chemisorption reactivity towards PMS (Zhao et al., 2022). Therefore, PMS is most likely to be initially adsorbed onto the Co nanocluster interface of Co/N-PC, promoting its activation and subsequent production of reactive oxygen species contributing to PAT degradation.

The projected density of states (PDOS) near the Fermi level of Co/N-PC was higher than that of Fe/N-PC, indicating that Co/N-PC achieved faster electron transfer and higher catalytic activity during the reaction (Fig. 6b) (Li et al., 2022). The corresponding *d*-band center relative to the Fermi level of Co–N_4 (−1.07 eV) and Co nanocluster (−1.40 eV) in Co/N-PC exhibited a downshift compared to that of Fe–N_5 in Fe/N-PC (−0.78 eV), which favoured the desorption of reaction intermediates (Du et al., 2024). After the adsorption of PMS, the PDOS between Co 3d and O 2p orbitals for Co/N-PC exhibited more overlaps than that

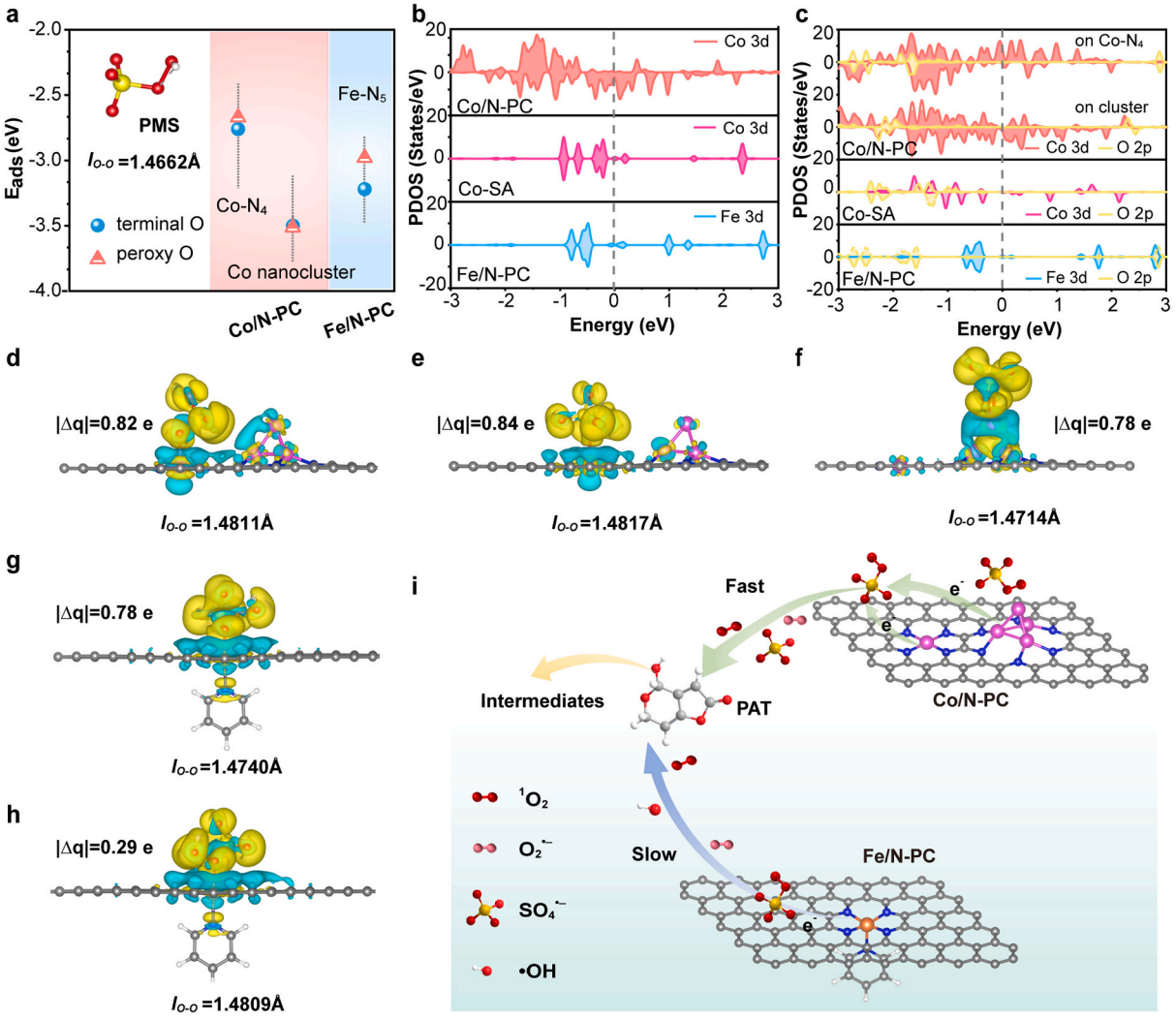

Fig. 6. (a) Adsorption energies of PMS on different metal active sites. (b) PDOS plot of Co 3d and Fe 3d in SAzymes. (c) PDOS plot of Co 3d, Fe 3d and O 2p orbitals in SAzymes/PMS systems. (d-h) Charge density differences for PMS configuration on metal active sites. Terminal O of PMS on the Co–N_4 site (d) and Fe–N_5 site (g), peroxy O of PMS on the Co–N_4 site (e) and Fe–N_5 site (h), terminal O and peroxy O of PMS on the Co nanocluster site (f). Where, yellow and blue regions represent electron accumulation and depletion, respectively. (i) Schematic illustration of the PAT degradation mechanisms of Co/N-PC and Fe/N-PC via PMS activation. (For interpretation of the references to colour in this figure legend, the reader is referred to the web version of this article.)

between Fe 3d and O 2p orbitals for Fe/N-PC, implying that Co/N-PC could activate PMS better through strongly coupled interactions between Co active centers and PMS (Fig. 6c) (Du et al., 2024). The results of difference charge-density analysis demonstrated that PMS could acquire electrons from Co–N_4, Co nanoclusters and Fe–N_5 sites, promoting efficient activation of PMS (Fig. 6d-h and Fig. S20) (Yang et al., 2022). The electron transfer quantities (|Δq|) calculated by Bader topology analysis, revealed that 0.82 e and 0.84 e were transferred from the Co–N_4 site to the terminal O atom and peroxy O atom, respectively. In contrast, the |Δq| from Fe–N_5 site to the terminal O atom was significantly higher (0.78 e) compared to the level of transfer to the peroxy O atom (0.29 e). Overall, the scale of electron transfer from Co active sites to PMS was greater than from Fe active sites, which aligned with the results of in-situ Raman analysis and chronoamperometry results. This enhanced charge transfer between the metal active site and PMS led to highly efficient reactive species generation and rapid PAT removal (Wang, Xiong, et al., 2023; Yang et al., 2023). The O–O bond length ($l_{O\text{-}O}$) of adsorbed PMS elongated from 1.4662 Å in free PMS to 1.4711 Å - 1.4817 Å, facilitating O–O bond breakage for the generation of radicals including $^1O_2$, ·OH and $SO_4^{\bullet-}$(Chen et al., 2022; Liang, Wang, et al., 2022; Wang, Gao, et al., 2023).

Furthermore, the role of Co nanoclusters in modulating the electronic structure of Co–N_4 was explored through comparisons with Co single-atoms (Co-SA), which possess only Co–N_4 sites (Fig. S21a). When Co nanoclusters coexisted with Co–N_4, the PDOS near the Fermi level and the overlaps between Co 3d and O 2p orbitals increased significantly as compared to the corresponding values observed in Co–N_4 alone (Fig. 6b and c). Furthermore, |Δq| transferred from the Co–N_4 site in Co/N-PC to the terminal O atom was higher than in Co-SA (Fig. S21b). These results indicate that the introduction of Co nanoclusters greatly enhanced electron density near the Fermi energy level in Co/N-PC, thereby facilitating effective PMS activation through electron transfer (Li et al., 2022). This highlights the high potential of custom-designed metal nanocluster configurations in optimizing the catalytic performance of SAzymes. Based on these observations, the proposed mechanism for the activation of PMS by M/N-PCs during PAT degradation is illustrated in Fig. 6i.

3.6. Application performance

In practical applications, the stability of a catalyst is critical. As shown in Fig. 7a and Fig. S22, the PAT degradation efficiencies of both

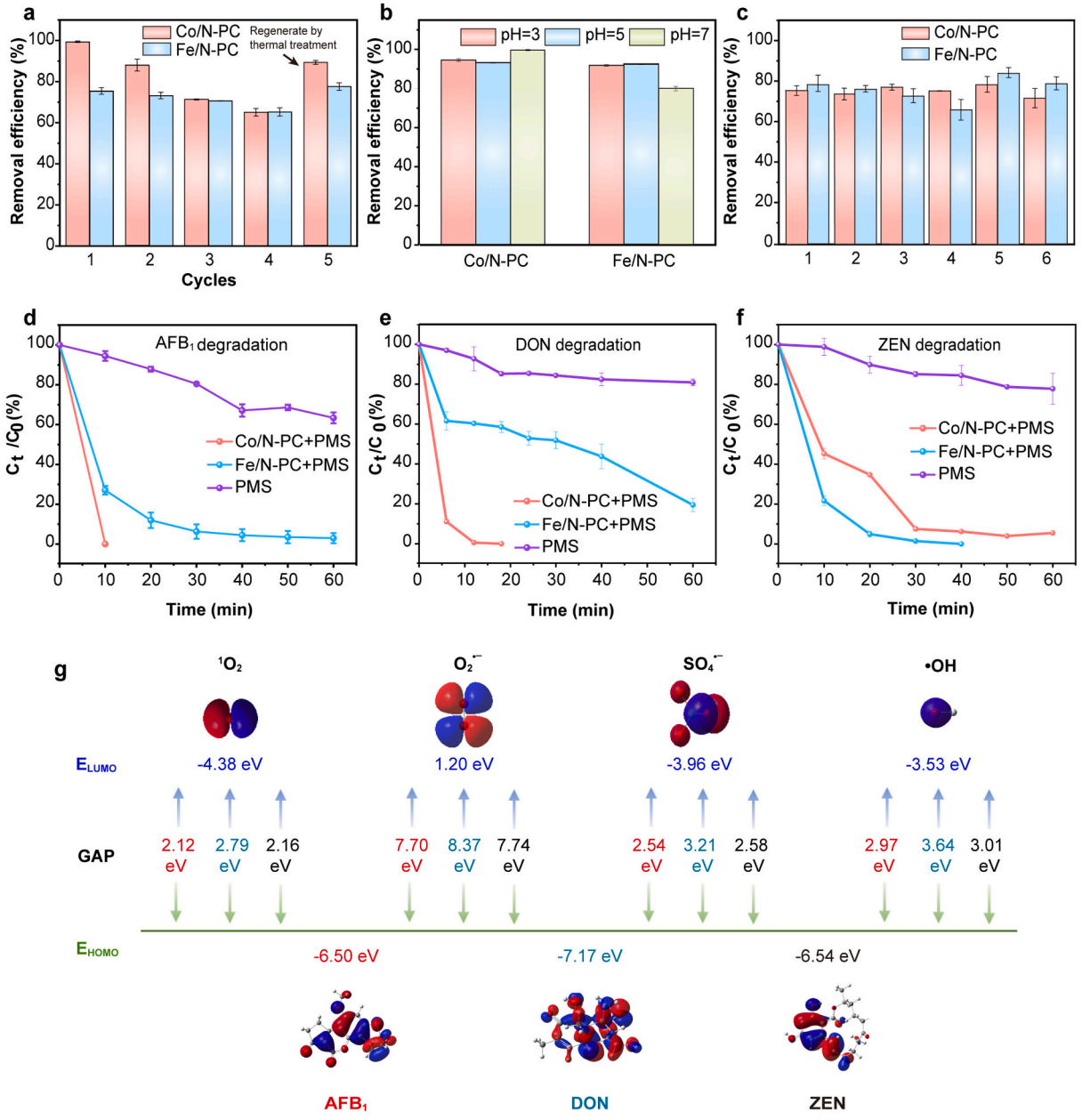

Fig. 7. (a) Reusability of M/N-PCs for PAT degradation. Conditions: [Cat.] =12.5 mg/L (Co/N-PC) or 50 mg/L (Fe/N-PC), [PMS] = 3.0 mmol/L, [PAT] = 2.5 mg/L, initial pH = 7.0. (b) Removal efficiency under different pH conditions. Conditions: initial pH = 3, 5, 7, other conditions are the same as for Fig. 7a. (c) Degradation efficiency in six apple juice samples. Conditions: [Cat.] = 200 mg/L, [PMS] = 6.0 mmol/L, [PAT] = 0.5 mg/L. (d-f) Degradation efficiencies of M/N-PC for AFB_1, DON and ZEN. Conditions: [PMS] = 3.0 mmol/L (DON) or 0.3 mmol/L (AFB_1 and ZEN), [AFB_1, DON and ZEN] = 2.5 mg/L, other conditions are the same as Fig. 7a. (g) Energy gap between the LUMO of reactive species and the HOMO of different mycotoxins.

Co/N-PC and Fe/N-PC catalytic systems declined with multiple cycles of use, but remained above 65 %, with their XRD patterns showing no significant changes. The gradual occupation of active sites by intermediates adsorbed onto the M/N-PC surface impedes interactions between active sites and PMS, which is a common issue in PMS-based heterogeneous catalysis (Cheng et al., 2023). Due to the stable anchoring of metal atoms within ZIF-8-derived porous carbon, the concentrations of Co and Fe ions leached from Co/N-PC and Fe/N-PC after 4 cycles of reuse were remarkably low, at 21.3 μg/L and 11.2 μg/L, respectively. The catalytic activity of Co/N-PC and Fe/N-PC could be recovered by thermal treatment, regenerating metal sites and demonstrating their high potential for reusability (Fig. 7a). Both Co/N-PC and Fe/N-PC displayed a good catalytic performance across the investigated pH range of 3–7, indicating the versatility of these catalysts for application in acidic and neutral environments (Fig. 7b). Table 1 presents a comparison of the M/N-PC/PMS catalytic systems proposed in this study, with commonly used biological enzyme and photocatalysis detoxification methods. Notably, Co/N-PC and Fe/N-PC achieved high degradation efficiencies (94.6 % and 91.8 %) within a short reaction time (1 h), significantly outperforming previously reported biological detoxification methods, which typically achieved degradation efficiencies of 40.0 % to 60.9 % after longer reaction periods (24 h) (Xing et al., 2023; Yan et al., 2024). Furthermore, the developed method required low catalyst dosages (12.5 mg/L and 50 mg/L), which were significantly lower than the required catalyst doses of other reported methods (>1000 mg/L) (Hu, Huang, & Peng, 2023; Lu, Yue, & Peng, 2022; Xing et al., 2023; Yan et al., 2024). These results highlight the practical applicability and efficacy of the proposed catalytic systems for

Table 1
Comparison of different methods for PAT degradation.

Catalysts	Methods	PAT amount (mg/L)	Catalyst amount (mg/L)	Degradation efficiency (%)	Time (h)	Ref.
PPL/Fe_3O_4@HMUiO-66-NH_2[a]	Biological detoxification	5	5000	60.9	24	(Yan et al., 2024)
Fe_3O_4@PDA@PEI@CgSDR[b]	Biological detoxification	20	50,000	~40.0	24	(Xing et al., 2023)
TiO_2 nanotubes	Ultraviolet photocatalysis	1	1000	~100	0.42	(Lu et al., 2022)
Nitrogen-doped chitosanTiO_2	Ultraviolet photocatalysis	0.5	1000	~100	1	(Hu, Huang, & Peng, 2023)
Co/N-PC	PMS detoxification	2.5	12.5	94.6	1	This work
Fe/N-PC			50	91.8		

[a] : porcine pancreatic lipase (PPL) modified magnetic hierarchical mesoporous UiO-66-NH_2; [b]: collected dopamine (DA)/polyethyleneimine (PEI)-modified magnetic Fe_3O_4 particles covalently linked free short-chain dehydrogenase/reductase (CgSDR).

PAT degradation.

PAT contamination frequently occurs in apple juice. Thus, the practical applicability of M/N-PC was evaluated in blank apple juice spiked with 0.5 mg/L of PAT, which is 10-fold higher than the permissible limit (50 μg/kg) (Hu, Huang, & Peng, 2023). The PAT degradation efficiencies achieved using the prepared M/N-PC catalysts (M = Co, Fe), ranged from 65.8 % to 84.2 % in different samples (including freshly squeezed and commercially packaged apple juice, Fig. 7c). Components such as malic acid, sugars, and hydroxymethylfurfural in apple juice can compete with PAT for active sites on the catalyst, thereby reducing the efficiency of PAT removal (Liang et al., 2022; Paimard et al., 2021; Yan et al., 2023). The proposed M/N-PC catalyst systems effectively removed a significant portion of PAT from all tested apple juice samples, demonstrating the high practical applicability of M/N-PC/PMS systems for PAT removal from contaminated products.

The ability of M/N-PC for broad-spectrum degradation of mycotoxins was further evaluated. As shown in Fig. 7d-f and Fig. S23, AFB_1, DON and ZEN could be degraded completely within 10–40 min. Remarkably, even with the use of a mere PMS (0.3 mmol/L), the developed SAzymes could reach a high efficiency in degrading AFB_1 and ZEN, highlighting their superior performance capabilities. As shown in Fig. 7g, similar to that of PAT, the GAP values between the LUMO of $^1O_2$ and the HOMO of these mycotoxins were the narrowest, suggesting that $^1O_2$ still played an important role. Moreover, the molecular sizes of AFB_1, DON and ZEN were 1.10 nm × 0.92 nm, 1.02 nm × 0.65 nm and 1.12 nm × 1.07 nm (Fig. S24), all of which can access the pore of M/N-PC to react with reactive species generated in situ for fast mass and electron transports. Compared with other reported methods in Table S4, the developed method of this work shows the advantages of low catalyst amount, high degradation efficiency and short treatment time, which further indicates that the method displayed excellent application prospects in the field of mycotoxin degradation.

4. Conclusions

In this study, Co- and Fe-based SAzymes were successfully synthesized, achieving enhanced catalytic degradation of mycotoxins. Co/N-PC, containing Co–N_4 and Co nanoclusters dual active sites, demonstrated the highest PAT degradation efficiency (99.4 % in 60 min) with minimal dosage, significantly outperforming Fe/N-PC, other reported natural enzymes and nanozymes. Four PAT degradation products were identified and displayed negligible toxicity to HEK 293T cells. DFT calculations revealed that the enhanced catalytic performance of Co/N-PC could be attributed to the introduction of Co nanoclusters, which modulated the electronic configuration of single Co atoms and enhanced the interaction between Co active sites and PMS, thereby facilitating the efficient generation of reactive species. M/N-PC exhibited good reusability, with broad pH tolerance (3–7) and good practical applicability in the degradation of PAT in apple juice. Additionally, the developed method exhibited a high efficiency for the degradation of AFB_1, DON and ZEN. In the mycotoxin degradation process, $^1O_2$ played a dominant role. This study elucidated the mechanism by which the metal active site structure of M/N-PC catalysts affected their catalytic efficiency, providing fundamental guidance for the rational design of SAzymes for mycotoxin degradation.

CRediT authorship contribution statement

Yaqi Zhang: Writing – original draft, Methodology, Investigation, Formal analysis, Data curation. **Huikang Lin:** Methodology, Investigation. **Lan Wang:** Investigation, Formal analysis. **Lijun He:** Formal analysis, Data curation. **Yong Man:** Formal analysis, Data curation. **Bingxuan Jia:** Methodology, Investigation. **Zheng Yan:** Data curation. **Shimo Kang:** Data curation. **Haijiao Xie:** Software, Methodology. **Aibo Wu:** Writing – review & editing, Supervision, Resources, Project administration.

Declaration of competing interest

The authors declare that they have no known competing financial interests or personal relationships that could have appeared to influence the work reported in this paper.

Acknowledgements

This work was supported by the National Science Fund for Distinguished Young Scholars of China (32025030), National Natural Science Foundation of China (U24A20473), China Postdoctoral Science Foundation (2023M743663) and Shanghai Post-doctoral Excellence Program (2023718).

Appendix A. Supplementary data

Supplementary data to this article can be found online at https://doi.org/10.1016/j.foodchem.2025.143852.

Data availability

Data will be made available on request.

References

Adegoke, T. V., Yang, B., Tian, X., Yang, S., Gao, Y., Ma, J., … Xing, F. (2023). Simultaneous degradation of aflatoxin B_1 and zearalenone by Porin and Peroxiredoxin enzymes cloned from Acinetobacter nosocomialis Y1. *Journal of Hazardous Materials, 459*, Article 132105. https://doi.org/10.1016/j.jhazmat.2023.132105

An, S., Zhang, G., Wang, T., Zhang, W., Li, K., Song, C., … Guo, X. (2018). High-density ultra-small clusters and single-atom Fe sites embedded in graphitic carbon nitride (g-C_3N_4) for highly efficient catalytic advanced oxidation processes. *ACS Nano, 12*(9), 9441–9450. https://doi.org/10.1021/acsnano.8b04693

Chen, Q., Liu, Y., Lu, Y., Hou, Y., Zhang, X., Shi, W., & Huang, Y. (2022). Atomically dispersed Fe/Bi dual active sites single-atom nanozymes for cascade catalysis and peroxymonosulfate activation to degrade dyes. *Journal of Hazardous Materials, 422*, Article 126929. https://doi.org/10.1016/j.jhazmat.2021.126929

Chen, Y., Jiang, B., Hao, H., Li, H., Qiu, C., Liang, X., … Liang, M. (2023). Atomic-level regulation of cobalt single-atom nanozymes: Engineering high-efficiency catalase mimics. *Angewandte Chemie International Edition, 62*(19), Article e202301879. https://doi.org/10.1002/ange.202301879

Cheng, C., Ren, W., Miao, F., Chen, X., Chen, X., & Zhang, H. (2023). Generation of Fe^{IV}=O and its contribution to Fenton-like reactions on a single-atom iron-N-C catalyst. *Angewandte Chemie International Edition, 62*(10), Article e202218510. https://doi.org/10.1002/ange.202218510

Diao, E., Hou, H., Hu, W., Dong, H., & Li, X. (2018). Removing and detoxifying methods of patulin: A review. *Trends in Food Science & Technology, 81*, 139–145. https://doi.org/10.1016/j.tifs.2018.09.016

Dong, C., Li, Y., Cheng, D., Zhang, M., Liu, J., Wang, … Ma, D. (2020). Supported metal clusters: Fabrication and application in heterogeneous catalysis. *ACS Catalysis, 10*(19), 11011–11045. https://doi.org/10.1021/acscatal.0c02818

Du, Q., Zhu, C., Yue, C., Cun, F., Du, Z., Liu, F., & Li, A. (2024). Anchoring atomically dispersed FeN_5 sites on porous and defect-rich biochar via cascade regulation strategy for efficient Fenton-like catalysis. *Applied Catalysis B: Environmental, 343*, Article 123570. https://doi.org/10.1016/j.apcatb.2023.123570

Feizollahi, E., & Roopesh, M. S. (2021). Mechanisms of deoxynivalenol (DON) degradation during different treatments: A review. *Critical Reviews in Food Science and Nutrition, 62*(21), 5903–5924. https://doi.org/10.1080/10408398.2021.1895056

Feng, M., Wu, X., Cheng, H., Fan, Z., Li, X., Cui, F., … He, G. (2021). Well-defined Fe-Cu diatomic sites for efficient catalysis of CO_2 electroreduction. *Journal of Materials Chemistry A, 9*(42), 23817–23827. https://doi.org/10.1039/d1ta02833b

Fu, J., Yue, X., Zhang, Q., & Li, P. (2024). Early warning technologies for mycotoxins in grains and oilseeds: A review. *Trends in Food Science & Technology, 148*, Article 104479. https://doi.org/10.1016/j.tifs.2024.104479

Gao, Y., Wu, T., Yang, C., Ma, C., Zhao, Z., Wu, Z., … Cheng, C. (2021). Activity trends and mechanisms in peroxymonosulfate-assisted catalytic production of singlet oxygen over atomic metal-N-C catalysts. *Angewandte Chemie International Edition, 60*(41), 22513–22521. https://doi.org/10.1002/anie.202109530

Hao, C., Li, T., Xie, Y., Zhou, J. X., Chang, F., Luo, L., … Hu, G. (2024). Synergistic catalysis of cobalt single atoms and clusters loaded on carbon film: Enhancing peroxymonosulfate activation for degradation of norfloxacin. *Advanced Functional Materials*. , Article 2414036. https://doi.org/10.1002/adfm.202414036

Hu, C., Huang, C., & Peng, B. (2023). Study on the mechanism of photocatalytic degradation of patulin in simulated apple juice. *Food Chemistry, 426*, Article 136592. https://doi.org/10.1016/j.foodchem.2023.136592

Hu, J., Zou, Y., Li, Y., Xiao, Y., Li, M., Lin, L., … Li, X. Y. (2023). Efficacy and mechanism of peroxymonosulfate activation by single-atom transition metal catalysts for the oxidation of organic pollutants: Experimental validation and theoretical calculation. *Journal of Colloid and Interface Science, 645*, 1–11. https://doi.org/10.1016/j.jcis.2023.04.093

Johns, L. E., Bebber, D. P., Gurr, S. J., & Brown, N. A. (2022). Emerging health threat and cost of Fusarium mycotoxins in European wheat. *Nature Food, 3*(12), 1014–1019. https://doi.org/10.1038/s43016-022-00655-z

Kolawole, O., Meneely, J., Petchkongkaew, A., & Elliott, C. (2021). A review of mycotoxin biosynthetic pathways: Associated genes and their expressions under the influence of climatic factors. *Fungal Biology Reviews, 37*, 8–26. https://doi.org/10.1016/j.fbr.2021.04.003

Li, J., Zou, Y., Li, Z., Fu, S., Lu, Y., Li, S., … Zhang, T. (2022). Modulating the electronic coordination configuration and d-band center in homo-diatomic Fe_2N_6 catalysts for enhanced poeroxymonosulfate activation. *ACS Applied Materials & Interfaces, 14*(33), 37865–37877. https://doi.org/10.1021/acsami.2c12036

Li, M., Yu, J., Liu, Q., Liu, J., Chen, R., Zhu, J., … Wang, J. (2022). Atomically dispersed $Fe\text{-}N_5$ sites anchored in porous N-doped carbon nanofibers for effective hydrogen evolution reaction. *ACS Sustainable Chemistry & Engineering, 10*(40), 13505–13513. https://doi.org/10.1021/acssuschemeng.2c04453

Li, R., Chen, T., Lu, J., Hu, H., Zheng, H., Zhu, P., & Pan, X. (2023). Metal-organic frameworks doped with metal ions for efficient sterilization: Enhanced photocatalytic activity and photothermal effect. *Water Research, 229*, Article 119366. https://doi.org/10.1016/j.watres.2022.119366

Li, X., Mitchell, S., Fang, Y., Li, J., Perez-Ramirez, J., & Lu, J. (2023). Advances in heterogeneous single-cluster catalysis. *Nature Reviews Chemistry, 7*(11), 754–767. https://doi.org/10.1038/s41570-023-00540-8

Li, Y., Li, Z., Shi, K., Luo, L., Jiang, H., He, Y., … Sun, G. (2023). Single-atom Mn catalysts via integration with Mn sub nano-clusters synergistically enhance oxygen reduction reaction. *Small, 20*(22), Article 202309727. https://doi.org/10.1002/smll.202309727

Li, Z., Ji, S., Xu, C., Leng, L., Liu, H., Horton, J. H., … Zhu, J. (2022). Engineering the electronic structure of single-atom iron sites with boosted oxygen bifunctional activity for Zinc-air batteries. *Advanced Materials, 35*(9), Article 2209644. https://doi.org/10.1002/adma.202209644

Li, Z., Li, K., Ma, S., Dang, B., Li, Y., Fu, H., … Meng, Q. (2021). Activation of peroxymonosulfate by iron-biochar composites: Comparison of nanoscale Fe with single-atom Fe. *Journal of Colloid and Interface Science, 582*, 598–609. https://doi.org/10.1016/j.jcis.2020.08.049

Liang, J., He, Q., Zhao, Y., Yuan, Y., Wang, Z., Gao, Z., … Yue, T. (2022). Synthesis of sulfhydryl modified bacterial cellulose gel membrane and its application in adsorption of patulin from apple juice. *LWT, 158*, Article 113159. https://doi.org/10.1016/j.lwt.2022.113159

Liang, X., Wang, D., Zhao, Z., Li, T., Gao, Y., & Hu, C. (2022). Coordination number dependent catalytic activity of single-atom cobalt catalysts for Fenton-like reaction. *Advanced Functional Materials, 32*(38), Article 2203001. https://doi.org/10.1002/adfm.202203001

Liu, H. Z., Shu, X. X., Huang, M., Wu, B. B., Chen, J. J., Wang, X. S., … Yu, H. Q. (2024). Tailoring d-band center of high-valent metal-oxo species for pollutant removal via complete polymerization. *Nature Communications, 15*(1), 2327. https://doi.org/10.1038/s41467-024-46739-1

Liu, L., Chen, Y., Li, S., Yu, W., Zhang, X., Wang, H., … Bian, Z. (2023). Enhanced electrocatalytic cathodic degradation of 2,4-dichlorophenoxyacetic acid based on a synergistic effect obtained from Co single atoms and Cu nanoclusters. *Applied Catalysis B: Environmental, 332*, Article 122748. https://doi.org/10.1016/j.apcatb.2023.122748

Lu, X., Yue, Z., & Peng, B. (2022). Preparation of TiO_2-nanotube-based photocatalysts and degradation kinetics of patulin in simulated juice. *Journal of Food Engineering, 323*, Article 110992. https://doi.org/10.1016/j.jfoodeng.2022.110992

Maneeboon, T., Roopkham, C., Mahakarnchanakul, W., & Chuaysrinule, C. (2024). Exploration of Pseudomonas knackmussii AD02 for the biological mitigation of post-harvest aflatoxin contamination: Characterization and degradation mechanism. *Journal of Stored Products Research, 109*, Article 102470. https://doi.org/10.1016/j.jspr.2024.102470

Meng, P., Li, J., Wang, P., Yang, G., Liu, W., Liang, S., … Sun, C. (2024). In-situ construction of Z-scheme silver phosphotungstate/polyimide photocatalysts and enhanced visible-light photocatalytic degradation of aflatoxin B_1 in vegetable oil. *Chemical Engineering Journal, 483*, Article 149153. https://doi.org/10.1016/j.cej.2024.149153

Mo, F., Song, C., Zhou, Q., Xue, W., Ouyang, S., Wang, Q., … Wang, J. (2023). The optimized Fenton-like activity of Fe single-atom sites by Fe atomic clusters-mediated electronic configuration modulation. *PNAS, 120*, Article e2300281120. https://doi.org/10.1073/pnas. 2300281120

Paimard, G., Mohammadi, R., Bahrami, R., Khosravi-Darani, K., Sarlak, Z., & Rouhi, M. (2021). Detoxification of patulin from juice simulator and apple juice via cross-linked Se-chitosan/L-cysteine nanoparticles. *LWT, 143*, Article 111146. https://doi.org/10.1016/j.lwt.2021.111146

Peng, L., Duan, X., Shang, Y., Gao, B., & Xu, X. (2021). Engineered carbon supported single iron atom sites and iron clusters from Fe-rich Enteromorpha for Fenton-like reactions via nonradical pathways. *Applied Catalysis B: Environmental, 287*, Article 119963. https://doi.org/10.1016/j.apcatb.2021.119963

Qiu, Y., Yan, J., Liu, X., Pang, Y., Ding, Y., & Lyu, F. (2024). A novel g-C_3N_4-SH@konjac glucomannan composite aerogel for patulin removal from apple juice and its photocatalytic regeneration. *Food Chemistry, 451*, Article 139421. https://doi.org/10.1016/j.foodchem.2024.139421

Ramalingam, S., Bahuguna, A., & Kim, M. (2019). The effects of mycotoxin patulin on cells and cellular components. *Trends in Food Science & Technology, 83*, 99–113. https://doi.org/10.1016/j.tifs.2018.10.010

Wang, F., Gao, Y., Fu, H., Liu, S. S., Wei, Y., Wang, P., … Wang, C. C. (2023). Almost 100% electron transfer regime over Fe-Co dual-atom catalyst toward pollutants removal: Regulation of peroxymonosulfate adsorption mode. *Applied Catalysis B: Environmental, 339*, Article 123178. https://doi.org/10.1016/j.apcatb.2023.123178

Wang, J., Han, G., Wang, L., Du, L., Chen, G., Gao, Y., … Yin, G. (2018). ZIF-8 with ferrocene encapsulated: A promising precursor to single-atom Fe embedded nitrogen-doped carbon as highly efficient catalyst for oxygen electroreduction. *Small, 14*(15), Article 201704282. https://doi.org/10.1002/smll.201704282

Wang, S., & Wang, J. (2023). Single atom cobalt catalyst derived from co-pyrolysis of vitamin B_{12} and graphitic carbon nitride for PMS activation to degrade emerging pollutants. *Applied Catalysis B: Environmental, 321*, Article 122051. https://doi.org/10.1016/j.apcatb.2022.122051

Wang, S., Wang, X., Penttinen, L., Luo, H., Zhang, Y., Liu, B., … Su, X. (2022). Patulin detoxification by recombinant manganese peroxidase from *moniliophthora roreri* expressed by *Pichia pastoris*. *Toxins, 14*(7), 440. https://doi.org/10.3390/toxins14070440

Wang, X., Xiong, Z., Shi, H., Wu, Z., Huang, B., Zhang, H., … Lai, B. (2023). Switching the reaction mechanisms and pollutant degradation routes through active center size-dependent Fenton-like catalysis. *Applied Catalysis B: Environmental, 329*, Article 122569. https://doi.org/10.1016/j. apcatb.2023.122569

Wang, Z., Zhu, C., Tan, H., Liu, J., Xu, L., Zhang, Y., … Lu, X. (2021). Understanding the synergistic effects of cobalt single atoms and small nanoparticles: Enhancing oxygen reduction reaction catalytic activity and stability for Zinc-air batteries. *Advanced Functional Materials, 31*(45), Article 2104735. https://doi.org/10.1002/adfm.202104735

Wei, L., Chen, S., Yang, X., Zhang, H., Mo, Z., Yang, J., & Wang, H. (2024). Synthesis of visible light driven spherical Bi_2MoO_6 structure for aflatoxin B_1 photodegradation. *Inorganic Chemistry Communications, 160*, Article 111886. https://doi.org/10.1016/j.inoche.2023.111886

Wu, S., Yang, Z., Zhou, Z., Li, X., Lin, Y., Cheng, J. J., & Yang, C. (2023). Catalytic activity and reaction mechanisms of single-atom metals anchored on nitrogen-doped carbons for peroxymonosulfate activation. *Journal of Hazardous Materials, 459*, Article 132133. https://doi.org/10.1016/j.jhazmat.2023.132133

Xia, D., Tang, X., Dai, S., Ge, R., Rykov, A., Wang, J., … Kang, F. (2022). Ultrastable Fe-N-C fuel cell electrocatalysts by eliminating non-coordinating nitrogen and regulating coordination structures at high temperatures. *Advanced Materials, 35*(5), Article 2204474. https://doi.org/10.1002/adma.202204474

Xiao, Z. J., Zhou, B. Q., Feng, X. C., Shi, H. T., Zhu, Y. N., Wang, C. P., … Ren, N. Q. (2023). Anchored Co-oxo generated by cobalt single atoms outperformed aqueous species from the counterparts in peroxymonosulfate treatment. *Applied Catalysis B: Environmental, 328*, Article 122483. https://doi.org/10.1016/j.apcatb.2023.122483

Xing, M., Chen, Y., Dai, W., He, X., Li, B., & Tian, S. (2023). Immobilized short-chain dehydrogenase/reductase on Fe_3O_4 particles acts as a magnetically recoverable biocatalyst component in patulin bio-detoxification system. *Journal of Hazardous Materials, 448*, Article 130986. https://doi.org/10.1016/j.jhazmat.2023.130986

Xu, B., Li, S., Zheng, L., Liu, Y., Han, A., Zhang, J., … Liu, H. (2022). A bioinspired five-coordinated single-atom iron nanozyme for tumor catalytic therapy. *Advanced Materials, 34*(15), Article 107088. https://doi.org/10.1002/adma.202107088

Xu, L. H., Liu, W., & Liu, K. (2023). Single atom environmental catalysis: Influence of supports and coordination environments. *Advanced Functional Materials, 33*(50), Article 2304468. https://doi.org/10.1002/adfm.202304468

Yan, X., Chen, K., Jia, H., Zhao, Q., Du, G., Guo, Q., … Yue, T. (2024). Infiltration of porcine pancreatic lipase into magnetic hierarchical mesoporous UiO-66-NH_2 metal-organic frameworks for efficient detoxification of patulin from apple juice. *Food Chemistry, 431*, Article 137172. https://doi.org/10.1016/j.foodchem.2023.137172

Yan, X., Dong, X., Zhao, Q., Du, G., Guo, Q., Yuan, Y., & Yue, T. (2023). Continuous flow removal of patulin by cysteine and porcine pancreatic lipase-modified hierarchical mesoporous zirconium metal-organic framework aerogel for apple juice treatment. *Chemical Engineering Journal, 475*, Article 146472. https://doi.org/10.1016/j.cej.2023.146472

Yang, J., Li, P., Duan, X., Zeng, D., Ma, Z., An, S., … He, Y. (2022). Insights into the role of dual reaction sites for single Ni atom Fenton-like catalyst towards degradation of various organic contaminants. *Journal of Hazardous Materials, 430*, Article 128463. https://doi.org/10.1016/j.jhazmat.2022.128463

Yang, X., Tan, M., Guo, J., Xiang, J., Yin, F., Deng, J., … Zhong, J. (2024). PdZn/CoSA-NC nanozymes with highly efficient SOD/CAT activities for treatment of osteoarthritis via regulating immune microenvironment. *Advanced Functional Materials*. , Article 2401963. https://doi.org/10.1002/adfm.202401963

Yang, Z., Yang, X., An, G., & Wang, D. (2023). Regulating spin state of Fe active sites by the P-doping strategy for enhancing peroxymonosulfate activation. *Applied Catalysis B: Environmental, 330*, Article 122618. https://doi.org/10.1016/j.apcatb.2023.122618

Yin, K., Peng, L., Chen, D., Liu, S., Zhang, Y., Gao, B., … Xu, X. (2023). High-loading of well dispersed single-atom catalysts derived from Fe-rich marine algae for boosting Fenton-like reaction: Role identification of iron center and catalytic mechanisms. *Applied Catalysis B: Environmental, 336*, Article 122951. https://doi.org/10.1016/j.apcatb.2023.122951

You, Y., Qiu, Y., Xu, H., He, R., Zhang, L., Wang, Z., & Xia, Y. (2024). Effective and food-grade detoxification of multiple mycotoxins using yeast expressed manganese peroxidases. *Food Bioscience, 59*, Article 103886. https://doi.org/10.1016/j.fbio.2024.103886

Zhang, H. C., Cui, P. X., Xie, D. H., Wang, Y. J., Wang, P., & Sheng, G. P. (2022). Axial N ligand-modulated ultrahigh activity and selectivity hyperoxide activation over single-atoms nanozymes. *Advanced Science, 10*(3), Article 2205681. https://doi.org/10.1002/advs.202205681

Zhang, Y., Sun, Y., Man, Y., Yuan, H., Zhao, R., Xiang, G., … Zhang, S. (2022). Highly efficient adsorption and catalytic degradation of aflatoxin B_1 by a novel porous carbon material derived from Fe-doped ZIF-8. *Chemical Engineering Journal, 440*, Article 135723. https://doi.org/10.1016/j.cej.2022.135723

Zhao, Z., Zhang, P., Tan, H., Liang, X., Li, T., Gao, Y., & Hu, C. (2022). Low concentration of peroxymonosulfate triggers dissolved oxygen conversion over single atomic Fe-N_3O_1 sites for water decontamination. *Small, 19*(7), Article 2205583. https://doi.org/10.1002/smll.202205583

Zhou, Z., Li, M., Kuai, C., Zhang, Y., Smith, V. F., Lin, F., … Shuai, D. (2021). Fe-based single-atom catalysis for oxidizing contaminants of emerging concern by activating peroxides. *Journal of Hazardous Materials, 418*, Article 126294. https://doi.org/10.1016/j.jhazmat.2021.126294

Zhu, E., Sun, C., Shi, C., Yu, J., Yang, X., & Xu, M. (2023). Isolated single-atom Fe-N_4O_1 catalytic site from a pre-oxidation strategy for efficient oxygen reduction reaction. *Chemical Engineering Journal, 463*, Article 142468. https://doi.org/10.1016/j.cej.2023.142468